Numerical Calculations of Adiabatic Invariants from MHD-Driven Magnetic Fields

D. E. da Silva[1], S. R. Elkington[1], X. Li[1], J. Murphy, M. K. Hudson[2], M. J. Wiltberger[2], A. A. Chan[3]

[1]Laboratory for Atmospheric and Space Physics, University of Colorado, Boulder, Colorado, USA
[2]High Altitude Observatory, National Center for Atmospheric Research, Boulder, Colorado, USA
[3]Department of Physics and Astronomy, Rice University, Houston, Texas, USA

Key Points:

- An algorithm with automated error control options is presented for calculating adiabatic invariants K and L^* on gridded, empirical, and MHD magnetic fields.
- Future research regarding the magnetic field model used for phase space density analysis is motivated through comparisons of empirical (T96, TS05) and MHD models (LFM, LFM-RCM).
- Code implementing the methodology presented here is provided open-source with this publication for free and open use.

Corresponding author: Daniel E. da Silva, daniel.dasilva@lasp.colorado.edu

Abstract
The adiabatic invariants (M, J, Φ) and the related invariants (M, K, L^*) have been established as effective coordinate systems for describing radiation belt dynamics at a theoretical level, and through numerical techniques, can be paired with in-situ observations to order phase-space density. To date, methods for numerical techniques to calculate adiabatic invariants have focused on empirical models such the Tsyganenko models TS05, T96, and T89. In this work, we develop methods based on numerical integration and variable step size iteration for the calculation of adiabatic invariants, applying the method to the Lyon-Fedder-Mobarry (LFM) global magnetohydrodynamics (MHD) simulation code, with optional coupling to the Rice Convection Model (RCM). By opening the door to adiabatic invariant modeling with MHD magnetic fields, the opportunity for exploratory modeling work of radiation belt dynamics is enabled. Calculations performed using LFM are cross-referenced with the same code applied to the T96 and TS05 Tsyganenko models evaluated on the LFM grid. Important aspects of the adiabatic invariant calculation are reviewed and discussed, including (a) sensitivity to magnetic field model used, (b) differences in the problem between quiet and disturbed geomagnetic states, and (c) the selection of key parameters, such as the magnetic local time step size for drift shell determination. The rigorous development and documentation of this algorithm additionally acts as preliminary step for future thorough reassessment of in-situ phase-space density results using alternative magnetic field models.

1 Introduction

The radiation belts of Earth have long been one of the most studied and central regions of what is now known as Earth's magnetosphere. High-energy charged particles trapped in the Earth's magnetic field follow stable orbits through the dynamical system of Earth's ring current. These charged particles are of notable concern to both geosynchronous/GPS satellites traversing the heart of the outer zone radiation belts and low-earth orbit satellites transiting the South Atlantic Anomaly. Harmful effects include charge buildup that will eventually result in pulsed discharges (a phenomena known as deep dielectric charging), and the related circuit interference. Such circuit interference is particularly dangerous as it may lead to command processors executing arbitrary routines, such as full-system resets or attitude adjustments (Baker et al., 1994, 1998; Baker, 1998; Shea & Smart, 1998). In addition, energetic particle interactions may mistrigger onboard circuit components into overdrawing current and irreversibly damaging the spacecraft's electronics. Because these effects may occur more intensely during periods of high radiation belt fluxes, a detailed understanding of the dynamics during such highly active periods is compelling. As modern infrastructure increasingly depends on such satellites, it becomes more and more critical to understand and predict the behavior of these high-energy particles to safeguard missions in these regions.

The specific paths trapped particles follow and how they become altered during geomagnetic storms is determined in part by the global configuration of the Earth's magnetic field. Our knowledge of Earth's magnetic field, and its variations during geomagnetic storms, can be quantified using either (a) empirical models capturing the large-scale configuration of the magnetosphere through fits of spacecraft data to mathematical models (N. Tsyganenko & Sitnov, 2007; N. Tsyganenko, 1995; N. A. Tsyganenko, 1989), or (b) based on dynamic, physics-based models of the Earth-Sun interaction, using spacecraft measurements for only the upstream solar wind boundary condition. Empirical models are typically classified as either internal or external models, where an "external" model is an additive deviation on top of an "internal" model. Broadly, external models capture effects from currents in the near-Earth space environment such as the ring current, tail current, and magnetopause currents (N. Tsyganenko, 2002), while internal models capture effects due to currents below the Earth's surface. Examples of internal models include a standard dipole and the International Geomagnetic Reference Field (Alken et

al., 2021; Langel, 1992). Examples of widely used external models in the modern era include the Tsyganenko family of models such as TS05, T96, and T89 (N. Tsyganenko & Sitnov, 2005; N. Tsyganenko, 1995; N. A. Tsyganenko, 1989). Dynamic models based on magnetohydrodynamics (MHD) driven by an upstream boundary condition in the solar wind are currently at a high high level of maturity, with prominent models in the community being the Lyon-Fedder-Moberry (LFM) code (Lyon et al., 2004), the Space Weather Modeling Framework (SWMF) (Tóth et al., 2012), the Open Geospace General Circulation Model (OpenGGCM) (Raeder et al., 2008), and the Grid Agnostic MHD for Extended Research Applications (GAMERA) (Zhang et al., 2019).

The canonical adiabatic invariants of a trapped particle are (M, J, Φ), derived from the Hamilton-Jacobi action integrals associated with the three periodic motions which trapped particles undergo (Haerendel, 1968; Schulz, 1996). The advantage of the adiabatic invariant coordinates is that of their nature as an essential state variable with respect to the changing global magnetic field. During a geomagnetic storm, the shape of the Earth's magnetic field will change in response to storm-time influences. In turn, the exact velocity $\mathbf{v}$ of trapped particles will change in response to the changed magnetic field. However, the adiabatic invariant coordinate (M, J, Φ) will remain constant provided (a) no work is done on the particle and (b) the global magnetospheric fields change sufficiently slowly. The adiabatic invariants are themselves a representation of the particle's velocity, being a function of both (v_x, v_y, v_z) velocity representation and the instantaneous magnetic field throughout the drift shell.

The community has widely adopted an alternative form of (M, J, Φ), denoted (M, K, L^*). The coordinates (MK, L^*) can be calculated directly from (M, J, Φ) (and are equivalently invariant provided no parallel forces exist along the magnetic field line), but provide several convenient and desirable properties over their predecessor. We also note that the first invariant M has a non-relativistic counterpart μ, related by the equation $M = \gamma\mu$, where γ is the Lorentz factor and μ is the magnetic moment of the particle. The magnetic moment μ is an adiabatic invariant only in non-relativistic scenarios.

The second invariants J and K are related through the following equations taken from Roederer & Zhang (2016),

$$K = J/(2\sqrt{2m_0 M}) = \int_{s_1}^{s_2} \sqrt{B_m - B(s)}\, ds. \tag{1}$$

The primary advantage of K is that it can be computed directly from a field line trace (depends on $\mathbf{B}$ alone), where as calculation of J requires tracking the particle's exchange of parallel and perpendicular momentum over a bounce.

The more convenient form of Φ is the dimensionless L^*, given by

$$L^* = 2\pi\mu_E/(R_E\Phi), \tag{2}$$

where μ_E is the magnetic moment of the Earth and R_E is the radius of the earth. L^* has the desirable property that in a dipole field, a particle found on an L-shell L will have $L^* = L$. This allows L^* to be used as a reference in comparison to L. Subsequently, the occurrence of particles found on an L-shell L with $L^* > L$ or $L^* < L$ therefore indicates that the magnetosphere has deviated from a dipole in such a way that the particle underwent outwards or inwards adiabatic motion, respectively, as a result of the magnetospheric reconfiguration. This is in contrast to the cause necessarily and solely being due to non-adiabatic transport as a result of work done by wave-particle interactions, such as betatron/Fermi acceleration (Boyd et al., 2018; Ukhorskiy et al., 2005; Green & Kivelson, 2004; Ingraham et al., 2001).

With such a coordinate for each particle, the phase space density $f(\mathbf{x}, \mathbf{p})$ is equivalent to $f(M, K, L^*, \varphi_1, \varphi_2, \varphi_3)$, where φ_1, φ_2, and φ_3 are the phases associated with each

periodic motion for M, K, and L^* respectively. In practice, the phase space distribution is largely not phase-dependent, so it is accepted to recast $f(M, K, L^*, \varphi_1, \varphi_2, \varphi_3)$ as the phase-averaged distribution $f(M, K, L^*)$ (pedantically, one should more specifically write $\bar{f}(M, K, L^*)$, but this is not entirely standard). The main advantage of the phase-averaged distribution is that it only has three dimensions compared to the six dimensions prior (not counting time). A continued discussion of the adiabatic invariants, their associated periodic motions, and the methods of computing M, K, and L^* can be found in *Section 2 - Algorithms and Methods.*

To study the charged particle populations of the radiation belts, particle flux distributions are measured in-situ by spacecraft instrumentation (e.g. Mauk et al., 2014; Escoubet et al., 2001). By relating count rates to instrument calibration parameters, the particle's momentum, and the spacecraft's orientation/position, velocity distributions in the form of $f(\mathbf{x}, \mathbf{p})$, $f(\mathbf{x}, \alpha, W)$, or $f(\mathbf{x}, \phi, \theta, W)$ can be collected. In these expressions, $\mathbf{x}$ is the position in space, where $\mathbf{p}$ is the particle relativistic momentum, α is a pitch angle between $\mathbf{p}$ and $\mathbf{B}$, W is a particle energy, and ϕ/θ are the azimuthal/elevation look directions. From these base forms of the distribution function, missions studying radiation belt dynamics will convert the distribution function to $f(M, K, L^*)$ to aide scientific analysis.

Currently in the radiation belt research community, the conversion of a spacecraft measured $f(\mathbf{x}, \mathbf{v})$ to $f(M, K, L^*)$ is done with empirical magnetic field models. Common codes include LANLStar (Yu et al., 2012), IRBEM (`https://prbem.github.io/IRBEM/`), SPENVIS (`https://www.spenvis.oma.be/`), LANLGeoMag (`https://github.com/drsteve/LANLGeoMag`) (Henderson et al., 2018), and direct particle tracing methods. Out of all these tools, only LANLGeoMag supports MHD model output, doing so by letting the user provide the global magnetic field in an unstructured array as points. Reasons most tools have not been adapted to MHD magnetic field models include the immediate availability of empirical models and the difficulties associated with performing the calculation using MHD magnetic field models. Such difficulties include (a) the more involved task of looking up $\mathbf{B(x)}$ due to non-uniform adapted grids, (b) the computational cost associated with running MHD simulations, and (c) the storage cost associated with preserving large MHD simulation output. Still, this is a missed opportunity, as the modeling capabilities of MHD simulation offers at the very least complimentary insight with empirical models for most studies using adiabatic invariants. This point will be expanded further in *Section 3 - Dependence of Invariants on Magnetic Field Model* and in *Appendix B - Comparison of Magnetic Field Models During the Main Phase.*

This work documents a rigorous treatment of the calculation of adiabatic invariants with MHD fields, presented as a stepping stone for exploratory modeling work in radiation belt dynamics using MHD simulation. As a mode of study to compliment (not replace) analysis using empirical fields, scientific inquiry using MHD simulation allows one to powerfully (a) access the otherwise-unavailable global state such as the density, flow velocity, pressure, and electric field and (b) experiment with impact of particular physics. In the past, access to the self-consistent global state from MHD simulations has allowed the community to answer questions on the now widely accepted importance of ULF waves on radial diffusion (Fei et al., 2006) and drift-resonant electron interactions (Elkington et al., 2002, 2003; Sarris et al., 2021). In addition, the work of Olsen et al. (2000) discussed the possibility of generating the peaks in phase space density profiles driven solely by Ultra Low Frequency (ULF) waves, and (Li et al., 2017) explored the calculation of radial diffusion coefficients using MHD modeling.

Broadly, MHD simulations offer the ability to inspect and evaluate wave propagation in the mHz frequency range, which are not included in empirical magnetic field models. Similarly, MHD simulation offers access to the global self-consistent physical variables mentioned, which are not available in empirical models like Tsyganenko. While empirical models of these variables do exist, they generally do not contain the wave prop-

agation, and are not self-consistent with the empirical magnetic field model. However, such variables are crucial to describing the full magnetospheric system. Furthermore, it is common for MHD simulation codes to have "optional" features, such as the inclusion of the Hall term (Huba, 1995) which can lead to qualitatively different results in the global magnetosphere (Bard & Dorelli, 2021). Other optional features include coupling the simulation with other models which cover aspects of the magnetospheric system known to be inaccurate with MHD alone (such as the ring current) (Heinemann & Wolf, 2001; Toffoletto et al., 2003).

The long-term principle question which this work aims to move towards addressing is that of what causes electron acceleration in the outer radiation belts. The leading method of addressing this is through the analysis of adiabatic invariant ordered phase space density measurements. In this style of analysis, different proposed mechanisms are reasoned using fundamental physics to generate different structural changes in the time-dependent $f(M, K, L^*; t)$, and spacecraft measured $f_{obs}(M, K, L^*; t)$ are compared against those anticipated structural changes. The leading two mechanisms to explain electron acceleration in the outer radiation belt are (a) local acceleration, driven by waves (such as chorus) which directly violate all three invariants, after which the particles are accelerated at their existing locations around $L < 6.6$ (these are sometimes called "growing peak" events), and (b) radial diffusion driven by processes (such as ULF wave interaction), which directly violate the third invariant, and transport particles from higher L-shells to lower L-shells, causing the particle energy to increase to adjust for its position in a stronger magnetic field while conserving first and second invariants. Radial diffusion is sometimes known as external acceleration. The result is a conclusion that the spacecraft measured $f_{obs}(M, K, L^*; t)$ appears indicative of a certain mechanism over others.

This method of analysis has been implemented using Polar spacecraft in-situ data in e.g., Green & Kivelson (2004) and Selesnick & Blake (2000), and Van Allen Probes in-situ data in e.g., Reeves et al. (2013) and Boyd et al. (2018). In Green & Kivelson (2004) and Boyd et al. (2018), a large number of events were analyzed and it was found that the structural changes in $f_{obs}(M, K, L^*)$ were most commonly aligned with local acceleration driven by chrorus wave activity. In addition, the work of Allison et al. (2021) provided a detailed analysis of the peaks in phase space density that corresponded to the multi-MeV electrons. It was noted in Boyd et al. (2018) that chorus acceleration was only the case for 87% of the events, leaving uncertainty as to alternative mechanisms which, while the minority, still play a role in electron acceleration overall. The question as to what happens when evidence for local acceleration is absent is complicated by the fact that during these times, multiple mechanisms may be occurring simultaneously, possibly with secondary interactions. In these studies, $f_{obs}(M, K, L^*)$ was computed using Tsyganenko empirical models, and Green & Kivelson (2004) warns as to the model-dependent nature of the calculation. Immediate questions to come from the methods developed here of extending adiabatic invariant calculation to MHD models are (a) are the previous results in the literature reproducible when the invariants are calculated from MHD models? and (b) what is available in the global MHD model context (such as wave activity and more generally ρ, $\mathbf{u}$, p, and $\mathbf{E}$) that can inform us as to what physics may be simultaneously occurring that affects the acceleration?

The calculation of the adiabatic invariants is developed here with the LFM global magnetospheric simulation code. LFM uses an adapted grid with cell density clustered around the inner magnetosphere, magnetosheath, and bow shock (Lyon et al., 2004). These areas were selected to provide finer detail in the field geometry where it is required. In this work we use a standalone version of LFM, and also a coupled model LFM-RCM, where RCM (Rice Convection Model) provides enhanced modeling of the ring current using a multi-fluid formalization more suited to that problem than MHD (Toffoletto et al., 2003). In this work we use LFM at "quad" resolution, which spans 106 x 96 x 128

cells along radial, azimuthal, and polar directions. The inner boundary for LFM simulations is at 2.1 R_E, with the full computational domain extending from +30 R_E to -300 R_E along the sun-earth line (SM x-axis) and from -150 R_E to +150 R_E along the SM y-axis and z-axis.

In *Section 2 - Algorithms and Methods*, we outline the numerical techniques developed to accomplish the adiabatic invariant calculation, as well as the tuning of key algorithmic parameters. In *Section 3 - Dependence of Invariants on Magnetic Field Model* we analyze a storm to note the differences between the MHD-driven LFM/LFM-RCM and the empirical Tsyganenko T96 and TS05 models. In this section, a time series of L^* is also presented and compared between the LFM and LFM-RCM models. In *Section 4 - Summary*, we summarize the work performed and anticipate future scientific advances.

In the Appendices, we provide supporting data to better understand this paper such as a summary of OMNI IMF Parameters during 2 October 2013 Storm, a comparison of magnetic field models during the main phase, an example of non-closed drift shell with features that complicate calculation of L^*, and an evaluation of alternative approaches for computing L^* such as with the International Geomagnetic Reference Field (IGRF) or using 2D polar cap integration.

2 Algorithms and Methods

Charged particles trapped in the radiation belts undergo three fundamental periodic motions. These period motions are gyration perpendicular to a magnetic field line, magnetic mirroring along a magnetic field line (bounce motion, sometimes called magnetic bottling), and azimuthal drift about the Earth. The first periodic motion, gyration, is the outcome of the continuous influence of the Lorentz force as it alters the direction of $v_\perp$, causing the particle to track a helix path. The second periodic motion, magnetic mirroring, is the outcome of the exchange of velocity between $v_\parallel$ and $v_\perp$ as the particle moves to increasing field strengths while conserving its kinetic energy and first invariant. For particles with a pitch angle outside a critical loss-cone threshold (Kallenrode, 2004; Tu et al., 2010), the particle will encounter a sufficiently strong field that will transfer any remaining parallel velocity into perpendicular velocity before reversing the particle in the direction from which it came. The third periodic motion, azimuthal drift, is caused by a combination of ∇B drift due to gradients in the magnetic field strength along the bounce path, and curvature drift due to the curvature of field lines along the bounce path (Fitzpatrick, 2022; Chen et al., 1984). Both of these influences act in a different direction based on the charge, and as a result protons and electrons azumithally drift in opposite directions. The surface covered by the particle as it bounces northward/southward along field lines, and its azimuthal drift about the Earth is called the particle drift shell. When combined together, these three structured and periodic motions (gyration, bouncing, and drifting) account for the trajectory of trapped particle when no outside work is being done.

The adiabatic invariants in this paper are calculated using numerical methods as a function of global magnetic field output from the LFM model and empirical models and initial particle velocity/position state.

Each adiabatic invariant corresponds to an integration over a path/surface associated with the respective periodic motion in the action integral. For the first invariant M this periodic motion is the path of a single gyration, for the second invariant K this is the bounce path, and for the third invariant L^* this is the drift shell. In the case of most geomagnetically trapped charged particles, the gyro radius is sufficiently small compared to the scale of structure in the magnetic field such that we can consider B constant over the entire gyration and thus no integration is required. We note that there are some scenarios where this is not the case, such as with electron motion under very

strongly curved field lines relative to the gyroradius (Artemyev et al., 2013). Therefore, calculation of the first invariant is trivial, but is discussed here for completeness.

The first adiabatic invariant, M, is calculated directly with the equation given in Roederer & Zhang (2016) and Murphy (2017). In this equation, p is the momentum, m_0 is the rest mass, $\bar{B}$ is the magnetic field strength averaged over a gyration (Chen et al., 1984), $p_\perp$ is the perpendicular momentum, and α is the particle's pitch angle.

$$M = \frac{p_\perp^2}{2m_0\bar{B}} = \frac{p^2 \sin^2(\alpha)}{2m_0\bar{B}} \tag{3}$$

The second adiabatic invariant is calculated using the bounce path. The bounce path is determined as a portion of the full field line trace done in both directions from the point in question. Given a starting point, the bounce path extends northward and southward, necessarily between the first occurrence of the magnetic mirroring strength B_m in each direction.

In this work, the field line trace is done by using the Runge-Kutta 4-5 method (Fehlberg, 1969). In mathematical terms, the trace of the magnetic field line is computed by solving

$$\mathbf{x}(0) = \mathbf{x}_0, \quad \dot{\mathbf{x}} = \frac{d\mathbf{x}(t)}{dt} = a\hat{\mathbf{B}} \tag{4}$$

where $\mathbf{x}(t)$ is the position of the field line trace at position t, $\mathbf{x}_0$ is the starting point of the trace, $\hat{\mathbf{B}}$ is the local direction of the magnetic field, and a is a constant to convert from units of magnetic field intensity to units of space over time (Kos et al., 2019). We note that we typically start the field line trace at the magnetic equator, in practice using Runge-Kutta 4-5 twice: once forward (for $t > 0$) to go northward and once backwards (for $t < 0$) to go southward. The trace is terminated when the inner (outer) boundary is reached, indicating a closed (open) field line.

The most common scenario for a field line in the inner magnetosphere is that the field strength is the strongest at the Earth's surface, declines monotonically towards a minimum value, and then increases again as the field line comes back towards the earth. In this case, the selection of any point along the same field line will produce the same bounce path. This is not the case for certain dayside field lines and associated values of B_m associated with drift shell splitting (Shabansky, 1971; McCollough et al., 2012). For these types of field lines, the field line intensity versus magnetic latitude will have two "wells" or local minima which will encapsulate the bounce path for sufficiently small B_m, whereas sufficiently large B_m will not be affected by this structure. Therefore, particles with sufficiently low B_m mirroring on such a field line may be trapped on a different bounce path depending on their starting location or bounce phase when entering the Shabansky region.

Because of this phenomenon, the bounce path is determined as a function of two parameters: the starting point and B_m. Specifically, the path is determined by iterating southwards and northwards along the field line trace until B_m is encountered. The starting point is not important if B at the starting point is less than B_m. When B_m is low enough for the particle to become trapped in one of the two bottom wells, a Shabansky orbit will occur.

Once the bounce path is determined, the next step is to integrate along the bounce path using the equation also derived in Equation 1 (Roederer & Zhang, 2016). In this equation, $\mathbf{B}(s)$ is the magnetic field strength at the position along the trace, B_m is the magnetic mirroring strength, and ds is the differential length along the trace path. Numerically, in this work this equation is integrated using trapezoidal integration with $ds \rightarrow \Delta s$ estimated as spatial distance between steps in the field line trace. The S.I. units of K obtained through this method are $\mathrm{km} \cdot \sqrt{\mathrm{nT}}$.

The final third adiabatic invariant, L^*, corresponds to the total magnetic flux outside the particle's drift shell. To calculate L^*, we first evaluate the drift shell for the particle. As the particle moves along its bounce path, it also undergoes an azimuthal drift based on its charge due to curvature of the field line and radial gradients in the field strength. The surface spanned by the particle's bounce motion and azimuthal drift is known as the drift shell. This surface necessarily never extends to either magnetic pole. It visually appears as a belt or ring around the earth. For a summary of the forces which contribute to the azimuthal drift, the reader is referred to Northrop (1963).

The classic way of calculating the drift shell is through a full particle trace. This involves solving a differential equation for the particle's position and momentum throughout its drift orbit and field line trace, for all points along its trajectory. However, this is computationally very expensive and most notably can be simplified using known physics. When it is known that the particle is trapped, the particle will necessarily move spatially inwards or outwards during the azimuthal drift to conserve its second invariant K corresponding to the fixed B_m (Roederer & Zhang, 2016). This key simplification forms the foundation of the Roederer method and allows us to determine the drift shell by iterating through magnetic local times (MLT's), and selecting the field line to find one which conserves K from the fixed B_m. This selection of the field line is significantly less computationally expensive than a full particle trace, though it leaves the question as to how many MLT's and how many field line searches to match K from B_m are required to accurately describe the drift shell.

Drift shell splitting is an important feature to capture in these calculations of the drift shell. The foundational work of Schulz & Lanzerotti (1974) established that drift shell splitting arises from either of two local time asymmetries in the magnetosphere: (a) local time asymmetries in the magnetic field, and to a lesser extent (b) from the presence of an electric field, such as the dawn-to-dusk electric field (Walsh et al., 2014). The Roederer method used in this work addresses the drift shell splitting from (a) but not (b), due to the electric field being a lesser source of drift shell splitting and the effects complicating the key simplifications that make the algorithm computationally efficient.

We present two methods for calculating the drift shell of a particle, the first which does so from fixed and equally spaced magnetic local times (MLT's) around Earth, and the second does so using automatically spaced MLT's. The automatically spaced MLT mode is backed by a Runge-Kutta algorithm which varies the spacing to meet user-specified absolute and relative error tolerances.

The overall equation used to calculate L^* in this work is,

$$L^* = \left(\frac{R_{inner}}{R_E}\right) \frac{2\pi}{\int_0^{2\pi} \sin^2(\theta_{inner}(\phi))d\phi}, \tag{5}$$

where R_{inner} is the inner boundary of the model, θ_{inner} is the northern most colatitude of the field line trace at the model inner boundary, and ϕ is the MLT as an angle between 0 and 2π. This is a modified Roederer & Zhang (2016) Equation 3.40, with a scaling of $Rinner/R_E$. This scaling is derived by extending the field line at the inner boundary of the model to 1 R_E using the dipole model, and in particular the equation $r = L\sin^2(\theta)$. When this equation is applied at the footpoint at both the model inner boundary location and at the magnetically connected surface footpoint, we can derive the equation,

$$\sin^2(\theta_{surface}) = \frac{R_E}{R_{inner}}\sin^2(\theta_{inner}), \tag{6}$$

where $\theta_{surface}$ is the northern most colatitude of the field line at the surface of Earth. Through this method, we evaluate L^* at 1 R_E, while simultaneously accommodating magnetic field models with inner boundaries above 1 R_E.

In the fixed and equally spaced mode, the drift shell field line is specified at N_{MLT} unique and equally spaced MLT's around Earth. We denote the MLTs as ϕ_i for $i = 1, 2, ..., N_{MLT}$.

First, a field line trace and accompanying $K(\phi_1, d_1)$ is found for the starting point at distance d from the magnetic equator.

Next, a field line search is done at each MLT to place the drift shell field line there. The search varies the candidate field line by way of the equatorial distance d, and continues to vary it until a field line is found which produces the desired $K(\phi_i, d_i) \approx K(\phi_1, d_1)$ using the same B_m. We note that in the case of equatorial mirroring particles, a shortcut exists, wherein one can instead search for d in $B_{min}(\phi_i, d) \approx B_{min}(\phi_1, d_1)$, a computationally simpler task because no field line trace is required, as this inherently satisfies the second invariant K when $K = 0$. This shortcut essentially amounts to finding an isoline of B_{min} around Earth.

To perform the search, candidate distances are tested using a linear search approach. A large step size is first used (called the initial step, equal to 0.05 R_E) to bracket the target, and then a smaller step size is used to refine the estimate (called the refined step, equal to 0.01 R_E). The stepping approach was used over bisection (as recommended in Murphy (2017)) because complex magnetospheres were found where the curve $K(\phi, d)$ vs. d possessed multiple matching K. When this occurred, the correct one (as determined by drift physics) is that which is closest to the previous drift shell field line. However, bisection would be unable to guarantee which matching solution would be obtained. For this reason, the algorithm was designed to gradually approach the target with carefully chosen step sizes. The sizes of both the major and refined steps were chosen to be smaller than the distances observed between multiple matching K in these complex magnetospheres.

When the iteration of refined steps identifies an interval of the refined step size holding d, the final interval is interpolated. A more controlled use of bisection was experimented with to replace this interpolation, where it would be used just over this final interval. The advantage would be that it could guarantee arbitrary error control between the target and acquired K values. However, we found that this approach resulted in code which was 2.5 times slower (with relative error set to 10^{-5}), and the impact on the final L^* was less than 0.1%. For this reason, it was deemed that the interpolation approach was sufficient.

In the automatically spaced MLT mode, the method for searching field lines at each MLT is similar. The key difference is that the MLTs selected are found while continuously solving the integral in Equation 5. Specifically, the integral is solved using Explicit Runge-Kutta method of order 4-5 (RK45) (Dormand & Prince, 1980), as implemented in the SciPy package (Virtanen et al., 2020), which selects MLTs along the integral bounds. Specifically, it solves the integral $D(\phi_{up}) = \int_0^{\phi_{up}} \sin^2(\theta_{inner}(\phi))d\phi$ through the differential equation $\frac{dD}{d\phi} = \sin^2(\theta_{inner}(\phi))$ and $D(0) = 0$, particularly seeking $D(2\pi)$ to arrive at the integral in Equation 5. The method is configured with user-specified relative and absolute error tolerances, which are used to automatically select where $\frac{dD}{d\phi}$ is evaluated based on its rate of change.

We note that the method algorithm is also parameterized by initial and maximum MLT spacings. These were selected through an experiment performed using the fixed equally-spaced MLT mode of the code. In this experiment, we looked at both simple (quiet-time) and complex (disturbed) magnetospheres with different magnetic field models, and varied the number of local times. We visually inspected these plots to look for where the calculation became stable. Calculation stability is determined by using a sufficiently high local time resolution (number of local time points) to sufficiently capture all necessary drift shell information. The results of this experiment can be found in Figure 1. We concluded that in the best case, the calculation becomes stable around four MLTs (the left column), and at the worst, around 16 (most of the right column). Therefore, we set the maximum spacing to $2\pi/4$ and the initial spacing to $2\pi/16$.

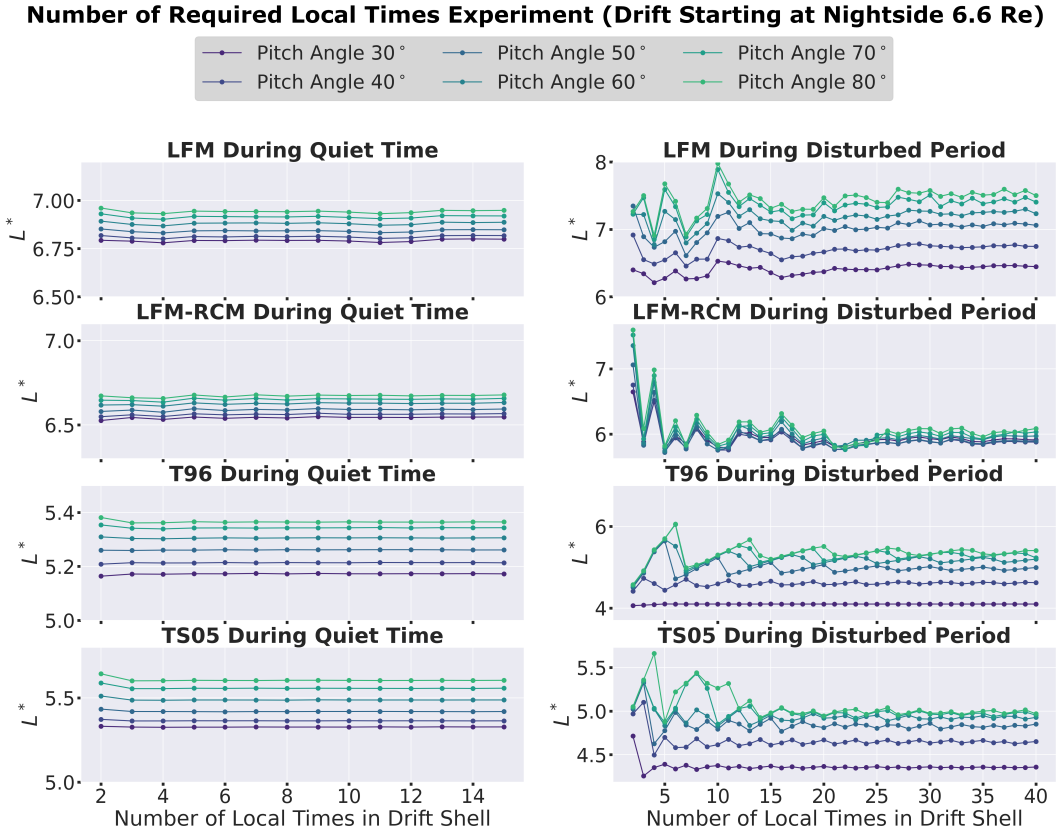

Figure 1. An experiment to investigate the minimum number of local times required in the drift shell to calculate L^* for simple (quiet time) and complex (disturbed period) magnetospheres. In this experiment, we increased the number of local times and visually inspected where the calculation became stable to determine at what point the number of local times is sufficient to model the drift shell.

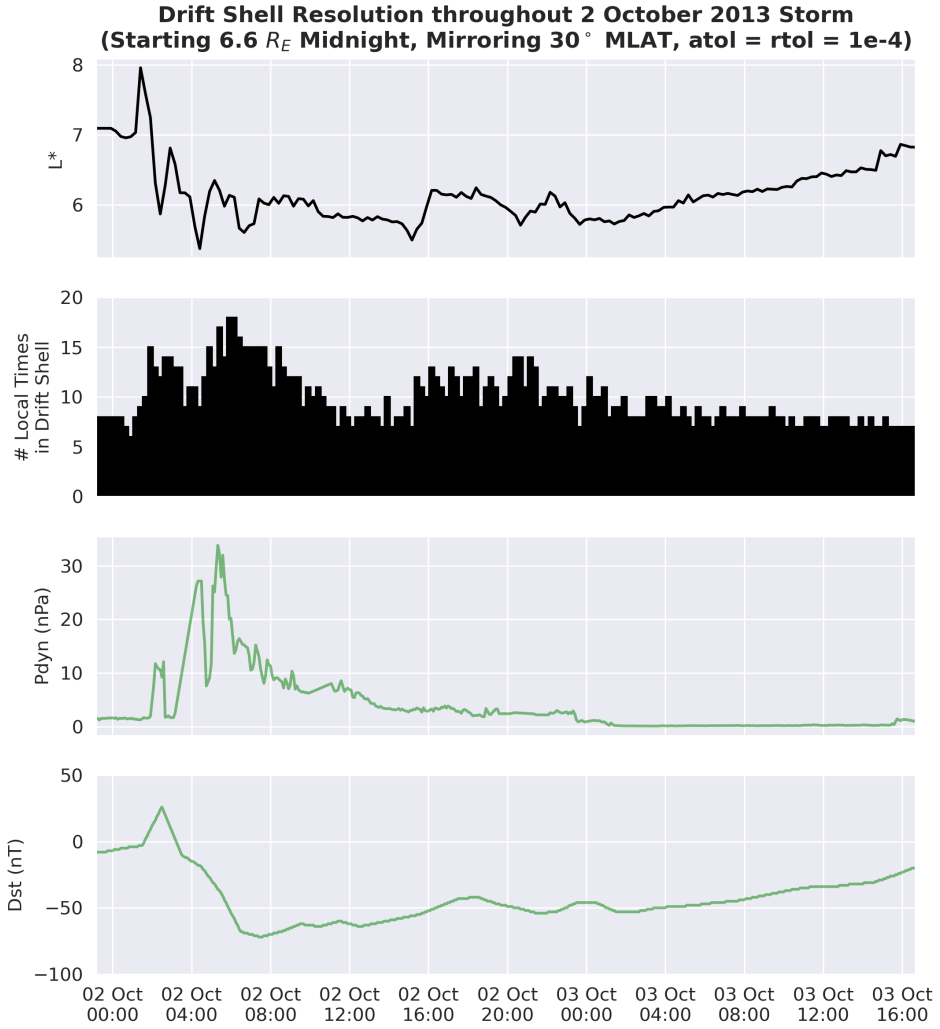

Figure 2. Changes in the automatically selected number of MLT's throughout the course of a geogmagnetic storm, when the automatically spaced MLT mode is used. In this plot, the absolute tolerance (atol) and relative tolerance (rtol) of the RK45 method was set to 10^{-4}.

We note that while the automatically spaced MLT mode provides desirable automated error control, it is usually 2-3 times slower than simply using the fixed equally spaced MLT mode with a safe spacing of $2\pi/16$. Therefore, we recommend that the fixed equally spaced MLT mode be used for "quicklook" initial data analysis, and the automatically spaced MLT mode be used for refined publication-quality results.

In Figure 2 we observe the automatically spaced MLT mode selecting a different number of MLTs throughout the course of a storm. The number of local times selected varies throughout the storm by a factor of two. The drift shells which required the highest number of MLTs to model occurred during the main phase of the storm. A second increase in drift shell complexity occurred later into the recovery phase, around where a secondary yet small drop in D_{st} occurred.

The automatically spaced MLT mode results in the completed integral; the fixed equally spaced MLT mode still requires numerical integration. This is done through trapezoidal integration after smoothing the integrand to counter any numerical noise from the drift shell calculation in $\theta_{inner}(\phi)$. The smoothing is performed with a cubic spline constrained with a periodic condition forcing the derivative of the integrand and the integrand itself equal at the boundary.

We review that the integral evaluated is the modified integral given in (Roederer & Zhang, 2016). Experiments were performed where the magnetic flux through the polar cap Φ was numerically integrated through

$$\Phi = \iint \mathbf{B} \cdot \hat{\mathbf{n}} \, dA, \tag{7}$$

with $\mathbf{B}$ provided by IGRF (Olsen et al., 2000). However, it was found that this approach changed L^* less than 1.5% throughout the outer radiation belt ($L^* > 3$), while being more computationally expensive, and therefore was not used. More information on this can be found in *Appendix D - Evaluation of Alternatives: IGRF and 2D Polar Cap Integration.*

3 Dependence of Invariants on Magnetic Field Model

In this section, we study the dependence of invariant calculation on magnetic field models using data from the 2 October 2013 geomagnetic storm. This is done to motivate future work which will investigate the effects of magnetic field model used to organize spacecraft-collected phase space density data. The models studied in this section are (a) the two MHD models LFM and LFM-RCM and the empirical models (b) T96 and TS05, all driven by solar wind conditions provided by 5-minute OMNI and the 5-minute QinDenton dataset for TS05 W parameters. In this section, we examine the adiabatic invariants calculated in each model, and discuss how features such as increased tail stretching, differing current structures, and off-equator dayside field line minima contribute to different invariant profiles.

Simulations of the 2 October 2013 geomagnetic storm were selected to provide a practical application for study. Through observation, the 2 October 2013 geomagnetic storm was classified as a G2 Moderate storm on the NOAA Space Weather Prediction Center (SWPC) scale, originating from a coronal mass ejection with an observed nominal solar wind speed of 600 km/s and observed strongly southward B_z with an observed nominal intensity of -19 nT. The LFM and LFM-RCM simulations were driven by L1 satellite observations of solar wind conditions from the WIND spacecraft (Gloeckler et al., 1995).

The structure of the inner magnetospheric fields holds key properties for understanding the orbit of geomagnetically trapped particles. The structure of the inner magnetospheric fields is determined from the currents in the magnetosphere and the Earth's

geomagnetic dynamo. The Earth's dynamo largely corresponds to the internal field, while the currents in the magnetosphere correspond to the external field. To characterize the external field, the intensity of the current contribution originating from the external field is calculated using Ampere's law.

$$\mathbf{J}_{ext} = \frac{1}{\mu_0} \nabla \times (\mathbf{B}_{model} - \mathbf{B}_{dipole}) \tag{8}$$

Visualization of this quantity across a meridional slice shows much finer level of current detail in the LFM/LFM-RCM than T96/TS05 as show in Figure 3. T96/TS05 leave absent many field-aligned currents around the poles and into the tail, and greatly simplify the cusp currents. Finally, all models show different interpretations of night-side plasmasphere currents, with this current largely absent in stand-alone LFM. These multiple models also show the footpoint of the cusp current at roughly the same location.

Field line traces are added to show differences in tail stretching and dayside compression. The traces start at magnetic latitudes in the inner boundary corresponding to the footpoints of field lines associated with L-Shells of $L = 1, 2, 3, \ldots$ of a dipole model. We see a drastically higher level of stretching in the T96/TS05 models, and similar levels of stretching between LFM and LFM-RCM.

Magnetic field models can be compared in reference to geosynchronous magnetometer data orbiting at 6.6 R_E in Figure 4. In this figure, data from the GOES-13 magnetometer is plotted alongside the magnetic field obtained from each model, taken at the ephemeris location of GOES-13. In the case of LFM/LFM-RCM, the magnetic field is linearly interpolated within a grid cell. In the case of T96/TS05, the model is evaluated directly at the GOES-13 satellite ephemeris.

This comparison illustrates agreement in B_x and B_y, but less so in the B_z. The disagreement in B_z is particularly emphasized during the main phase and early recovery period of the storm. During the extended recovery period, the shape of B_z is broadly retained throughout the recovery and during brief fluctuation (10/03, 18:00). We note that in LFM and LFM-RCM, B_z is offset from the observation even though the fluctuations match. This offset in B_z has been discussed in the literature and is understood to be related to tail stretching and LFM's tendency to produce weaker-than-reality currents in the plasma sheet (Wiltberger et al., 2000). A zoomed version of this plot is included in *Appendix B - Comparison of Magnetic Field Models During the Main Phase*, which highlights the differences in B_z during the main phase of the storm up to and slightly after the storm's minimum D_{st}.

The differences in B_z between approximately 2 October at 4:00 and 16:00 are now discussed in the context of Equations 1 and 5. When calculating K in this context, the parameters dependent on the magnetic field model are the mirror points s_1 and s_2, and the magnetic field strength along the bounce path, B(s). In our comparison, we see that $|B|$ differs between models by as much as 50%. Smaller $|B|$'s along the bounce path would make the bounce path longer (required to go to higher MLATs to reach B_m), and $B(s)$ smaller along the bounce path. These errors would propagate to errors in K, which would then propagate into an error in the drift shell and in turn L^*.

To illustrate this further, a profile of K is compared between models in Figure 5. In this visualization, the color at a particular location corresponds to the K associated with a particle mirroring on that magnetic field line at that magnetic latitude. The solid black lines are field line traces are each L-shell, and the dashed black lines are isolines of constant K. This plot was constructed with a 2D grid with linear spaced distances and mirroring magnetic latitudes. For each grid point, K was calculated for particles mir-

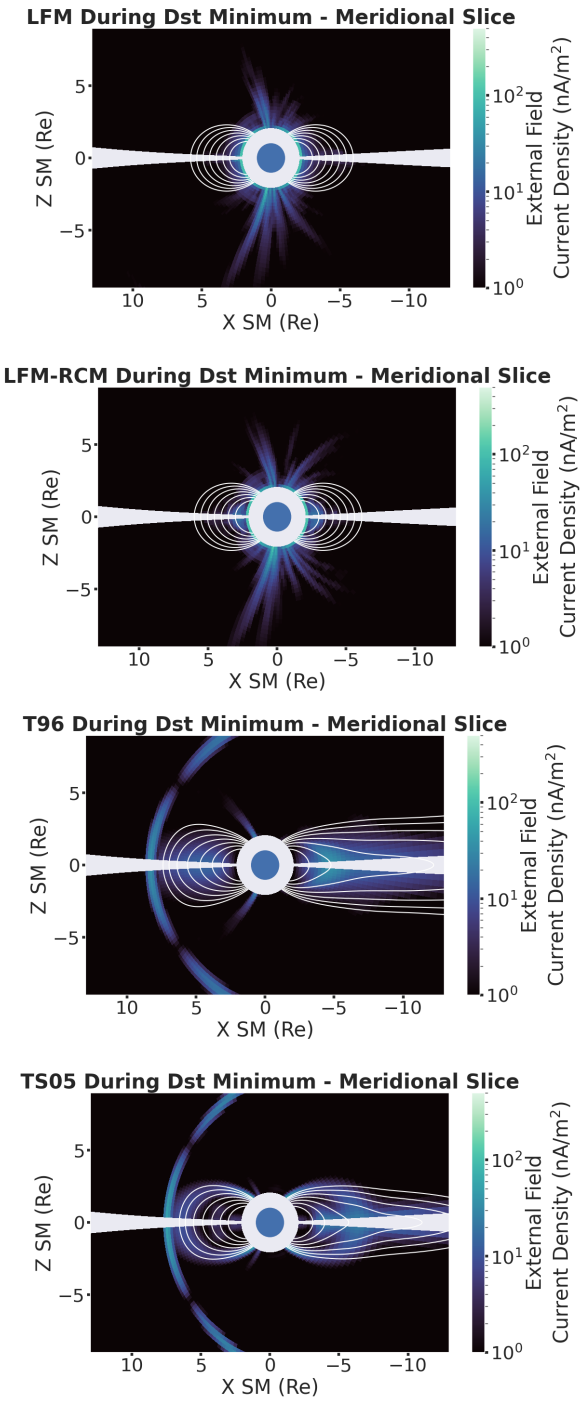

Figure 3. External field current density contribution from different magnetic field models in the inner magnetosphere, during D_{st} minimum of the 2 October 2013 storm. This quantity is calculated using Ampere's law in Equation 3. Field line traces are overlaid starting at magnetic latitudes on the inner boundary corresponding to the footpoint of field lines associated with L-Shells of $L = 1, 2, 3, ...$ in a dipole model. In this plot, we note the finer detail of current structures in LFM and LFM-RCM, increased tail stretching in T96 and TS05, and the differences in night-side plasmasphere currents between all models.

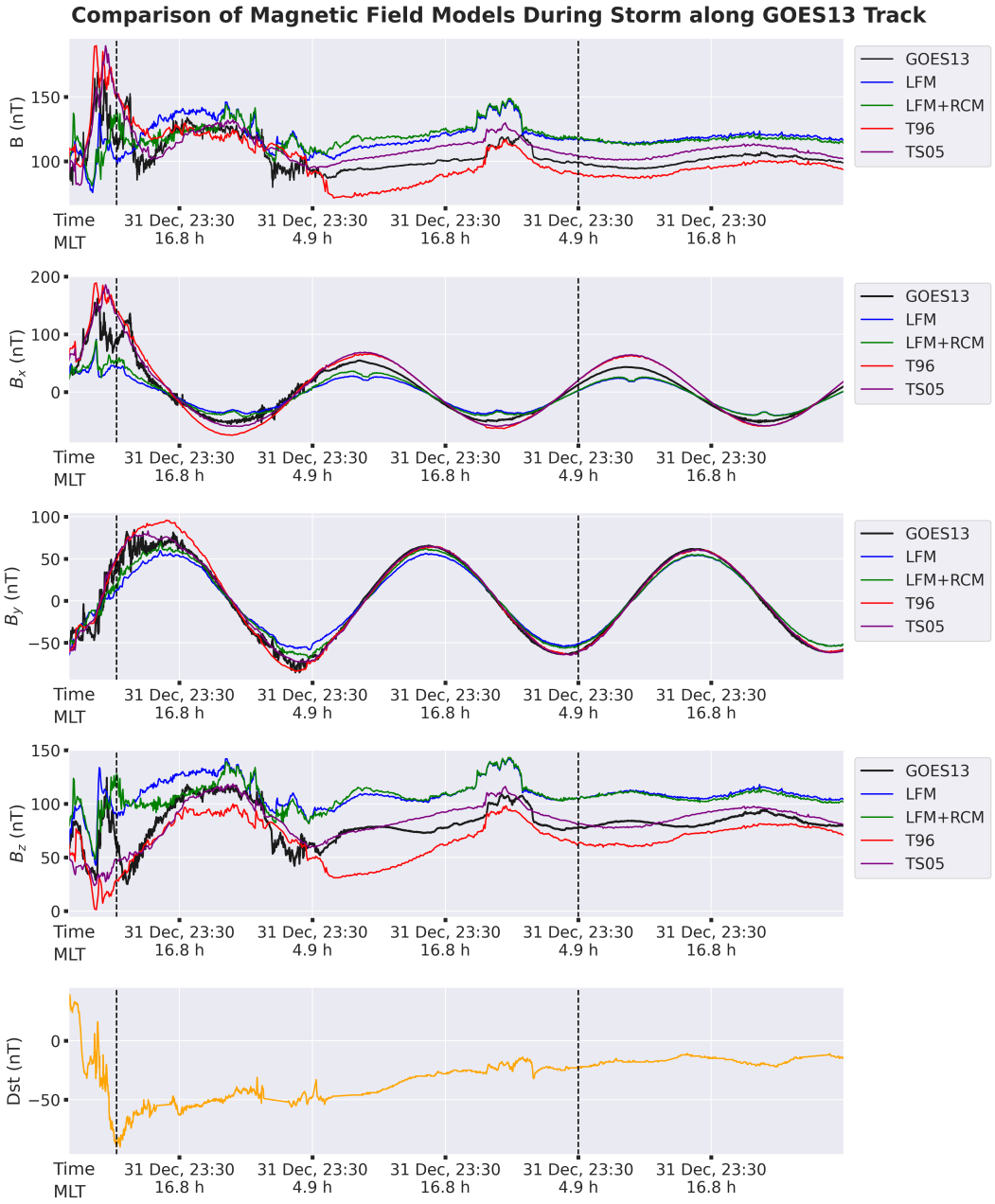

Figure 4. Magnetic field models compared to geosynchronous GOES-13 magnetometer data at 6.6 R_E. The magnetic field components are plotted in GSM coordinates. This comparison illustrates good agreement with observation in the B_x and B_y components for all models, and then much disagreement in the B_z particularly during the main phase and early recovery period of the storm. The two vertical bars identify the minimum D_{st} (left vertical bar), and the quiet time periods referenced in Figure 1 and Figure 5.

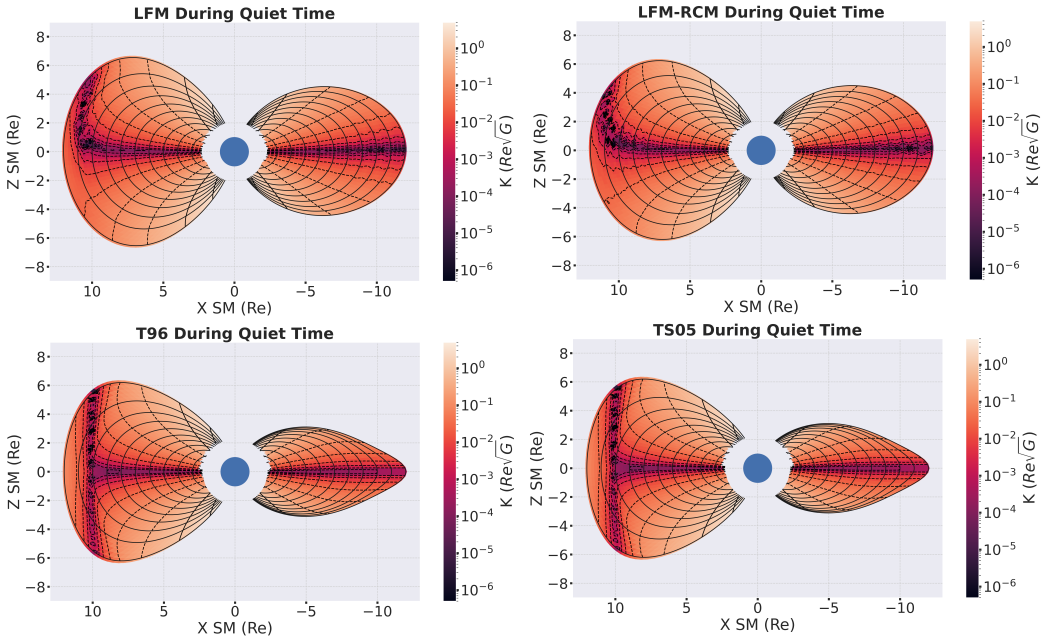

Figure 5. Profile of K (quiet times on left, disturbed period on right). In this visualization, the color at a particle location corresponds to the K associated with a particle mirroring on that magnetic field line at that magnetic latitude. The color of the plot is the value of K for a particle mirroring on that magnetic field line at that magnetic latitude. The dashed lines are isolines of constant K. The solid black lines are field line traces for each L-shell. A prominent feature of this plot is the abrupt upward trend for the $K = 0$ line on the dayside, which is slightly different shape for each model. This is due to the moving location of the minimum field intensity further out into the dayside.

roring at the given magnetic latitude, starting at the point $(d, 0, 0)$ for distance d in the SM coordinate system.

A prominent feature of this plot is the abrupt upward trend for the K=0 lines on the dayside. This is due to the moving location of the minimum field intensity further out into the dayside. The change in the minimum field intensity is understood to be due to the influence of the solar wind, the dipole tilt, Shabansky orbits and off-equatorial minima.

The K profile holds implications for the study of equatorially mirroring test particle simulations. An assumption of equatorially mirroring test particle simulations is that $K = 0$ at B_{min}, which also coincides with the magnetic equitorial plane in the simulation. This property is shown here to generally hold within $\approx 10\ R_E$, on both the dayside and nightside, but generally not farther out. This observation is reassuring for the ability for test particle simulations to model the outer radiation belt largely contained within this range. We notice that the shape of this $K = 0$ line is slightly different between each model, with T96 particularly having an out-of-trend shape.

In Konstantinidis & Sarris (2015), magnetic field models were compared through the analysis of L^* vs increasing distances into the tail. The authors of this work report differences in adiabatic invariants between various empirical model tools, with variations in L^* as much as 5% at 6 R_E and 30% at 8 R_E. The tools examined by those authors included LANLStar (Yu et al., 2012), IRBEM (`https://prbem.github.io/IRBEM/`), SPEN-

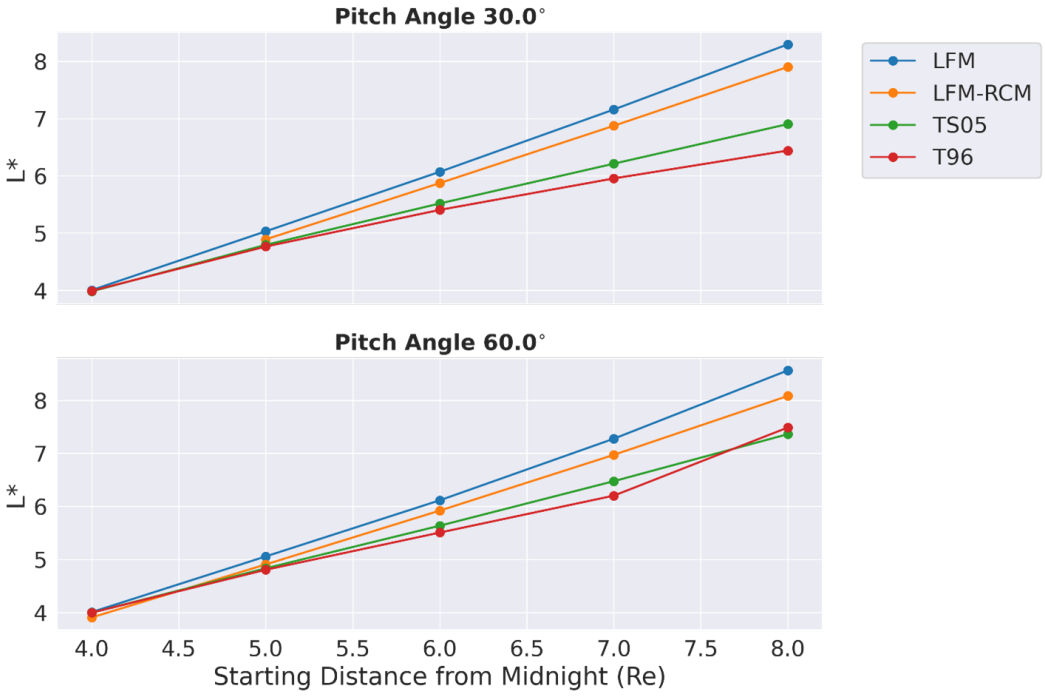

Figure 6. Calculation of L^* at increasing distances into the tail between magnetic field models during quiet-time conditions. We note that LFM and LFM-RCM contain less stretching than the T96 and TS05 models, and therefore starting the same point in the represent notable different values of K. This plot reflects a similar visualization as found in (Konstantinidis & Sarris, 2015) where LANLstar, IRBEM, SPENVIS, and a particle tracer were compared.

VIS (`https://www.spenvis.oma.be/`), and a particle tracer. An analogous comparison is presented here using the models studied in this paper during a quiet magnetosphere, shown in Figure 6. In each plot, one can see separation between the MHD (LFM and LFM-RCM) and the empirical models (TS05 and T96). This is understood to be because the MHD models contain less stretching than the empirical models, therefore yielding different K.

Finally, in Figure 7 we see L^* calculated at increasing distances into the tail and two mirroring magnetic latitudes (15° and 30°). The OMNI IMF parameters during this storm are provided in *Appendix A*. The most variation in L^* over the course of the storm occurs at larger distances into the tail, where the influence of the external field over the dipole is the greatest. It is noted that during the main phase of the storm, the drift shells associated with $d = -8\ R_E$ are largely not closed and do not allow the algorithm to converge. An example of a magnetosphere which contains such not closed drift shells can be found in *Appendix C* Figure C1. A zoomed in plot displaying a comparison during the main phase of the storm between GOES measurements of B_z and the corresponding model B_z at the GOES ephemeris for LFM, LFM-RCM, T96, and TS05 can be found in *Appendix B* Figure B1.

There are interesting differences between LFM and LFM-RCM during the beginning of the recovery phase on 2 October at 12:00 when the large magnetospheric field disturbances have completed but ring current enhancement continues. The decline in L^* for the $d = -8\ R_E$ lines is similar, but shows a much different shape around 2 October at 18:00. This is likely due to the more detailed ring current modeling that RCM

provides that acts as a feedback, providing pressure modification to the MHD solution by LFM. The fluctuation in L^* around 3 October at 18:00 corresponds with a denser burst of solar wind traveling at the same velocity as the solar wind preceding and following. Both magnetic field models produce comparable L^*'s that reflect the magnetosphere's response to this small/brief solar wind density fluctuation.

4 Summary

In this paper we present a rigorously developed methodology for calculating adiabatic invariants in MHD-driven fields, starting with those from LFM. Our methodology follows groundwork first laid out in Roederer & Zhang (2016) and further refined in Murphy (2017). The rigorous development and documentation of this algorithm is a contribution to the research community as groundwork preceding the code's use in scientific studies.

In addition to the methodology, this paper presented evidence to justify the effort spent developing tools for the calculation of adiabatic invariants on MHD-driven fields. A detailed analysis of meridional current derived from LFM, LFM-RCM, T96, and TS05 was presented and showed differences between the models that should be considered to establish confidence in results that use L^*. In particular, we showed a much higher level of detail in current complexity in the MHD-driven models compared to the empirical models.

Calculation of L^* over the course of the 2 October 2013 storm for LFM and LFM-RCM showed that differences in L^* exist primarily at larger L^* in the magnetosphere where the external field's influence over the dipole grows. The time series of the L^* calculation between LFM and LFM-RCM showed influence of the ring current modeling as a feedback mechanism that effects L^*.

These tools are developed with the intent to enhance the capability of modeling studies using L^* , as well as extending the ability to accurately organize in-situ data using adiabatic invariants. In this paper we noted the difference in L^* structure based on whether LFM was coupled with the RCM model. A rich history of magnetospheric simulation has explored different variants of the MHD equations (such as Hall and Multi-Fluid), as well as complex many-model coupling (Merkin 2022; Pham et al. 2022). By establishing methodology and code to analyze the dynamics of trapped particles under simulated magnetospheres, we begin a period of science where the impacts of modeling choices on trapped charged particle dynamics can be studied.

5 Data Availability

Code which implements the algorithms presented in this paper at the time of publication is made openly available on Zenodo at `https://[will-be-uploaded-upon-acceptance]`. Future updates of the code will be made available at `https://github.com/ddasilva/dasilva-invariants`. A package home page which includes both API documentation and usage examples is currently available online at `https://dasilva-invariants.readthedocs.io/`. The authors recommend that future users of the package check the home page and use the latest available version for their research, and that publications which using the package acknowledge it through citation of this manuscript.

Data from the OMNI database is available from OMNIWeb and NASA Goddard Spaceflight Center (GSFC) Space Physics Data Facility (SPDF) at `https://omniweb.gsfc.nasa.gov/`. Data from the GOES13 magnetometers is available online from the National Centers for Environmental Information (NCEI) at `https://www.ngdc.noaa.gov/stp/satellite/goes/`. Runs of LFM are available on-demand from the Community Coordinate Modeling Center's (CCMC's) Run-on-Request System at `https://ccmc`

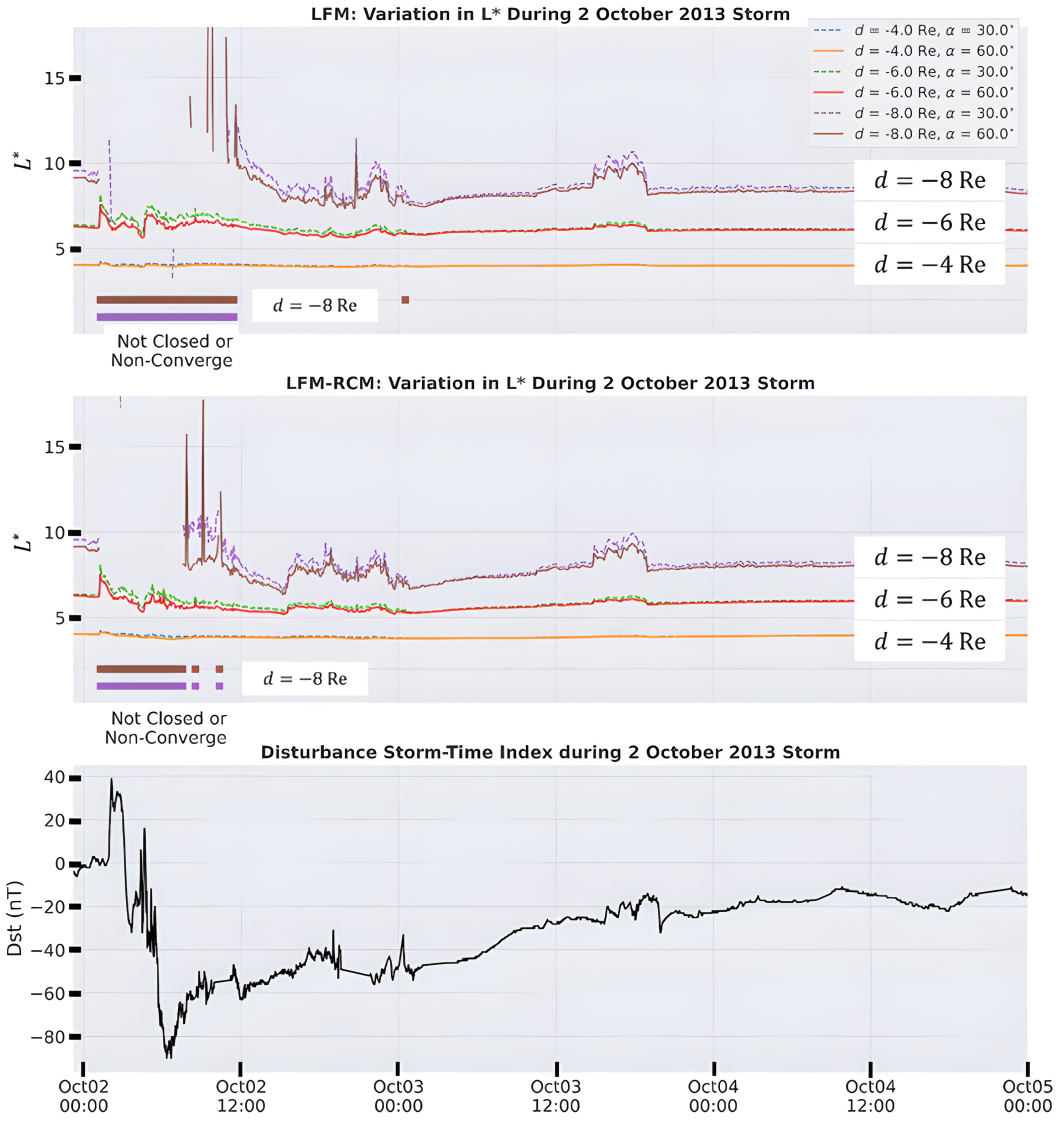

Figure 7. Values of $L*$ calculated at various distances into the tail during the 2 October 2013 Storm. We note that during the main phase of the storm many of the drift shells are not closed and resulted in L^* calculations that did not converge. Furthermore, the biggest deviations of L^* from the dipole L^* occur farther into the magnetosphere where the external field holds greater influence over the dipole field.

.gsfc.nasa.gov/models/LFM~LTR-2_1_5/. The QinDenton dataset used for TS05 W parameters can be found at http://mag.gmu.edu/ftp/QinDenton/5min/merged/latest/.

Acknowledgments

The authors would like to thank (a) the University Corporation for Atmospheric Research (UCAR) and the associated High Altitude Observatory (HAO) for providing supercomputing resources used for the development of this manuscript, and (b) the NASA Future Investigators in NASA Earth and Space Science and Technology (FINESST) program for providing funding to complete this research.

Appendix A OMNI IMF Parameters during 2 October 2013 Storm

The IMF parameters propagated from L1 observations to the bow shock by the OMNI data product show the type of incoming solar wind during the storm as seen in Figure A1. This data was taken from the OMNI database (https://omniweb.gsfc.nasa.gov/). The CME-driven enhancement associated with abrupt increases in IMF number density and velocity occurs around 2 October at 06:00. Following this abrupt increase, the IMF number density reduced back down to a nominal state, while the solar wind speed gradually decreases over the next few days. Around 3 October at 18:00 is a "blip" of increased IMF number density with in-trend IMF velocities, that in turn increases the IMF dynamic pressure and affects L^* in the tail, as shown in Figure 7.

Appendix B Comparison of Magnetic Field Models During the Main Phase

In the 2 October 2013 storm analyzed in this paper, a comparison between the considered model's field predictions at GOES-13 was presented in combination with GOES-13 data in Figure 4. What is not immediately obvious from Figure 3 are the differences during the main phase of the storm. A zoomed portion of that plot during the main phase of the storm (up until and slightly after D_{st} minimum) is presented here, with particular focus on the B_z panel.

In this plot, we notice that the shape of B_z observed by GOES-13 is much better captured by the MHD models (LFM and LFM-RCM) than by the empirical models (T96 and TS05). Up until around 2 October at 04:30, all models show a gradual decrease in B_z, though the arc is more closely captured by the MHD models. However, only the MHD models capture the increase in B_z following this period. In the final hour of this plot, GOES-13 observations show B_z reducing again, which is not captured well by any of the four models.

Appendix C Example of Non-Closed Drift Shell

The calculation of L^* is only valid for trapped particle radiation and during times where the magnetic field is changing slowly compared to the drift period. However, during particular disturbed periods of the magnetosphere particles that were previously trapped will no longer be trapped and will escape along open field lines. Furthermore, during particularly disturbed periods the magnetic field will change much faster than the drift period and using one snapshot of the magnetospheric magnetic field will be insufficient to describe the particle's trajectory.

We illustrate one example of a particularly disturbed magnetosphere here, illustrated by an equatorial slice of the TS05 empirical model during the 2 October 2013 storm. In this plot, the colors correspond to the log-scale magnetic field intensity, and the black

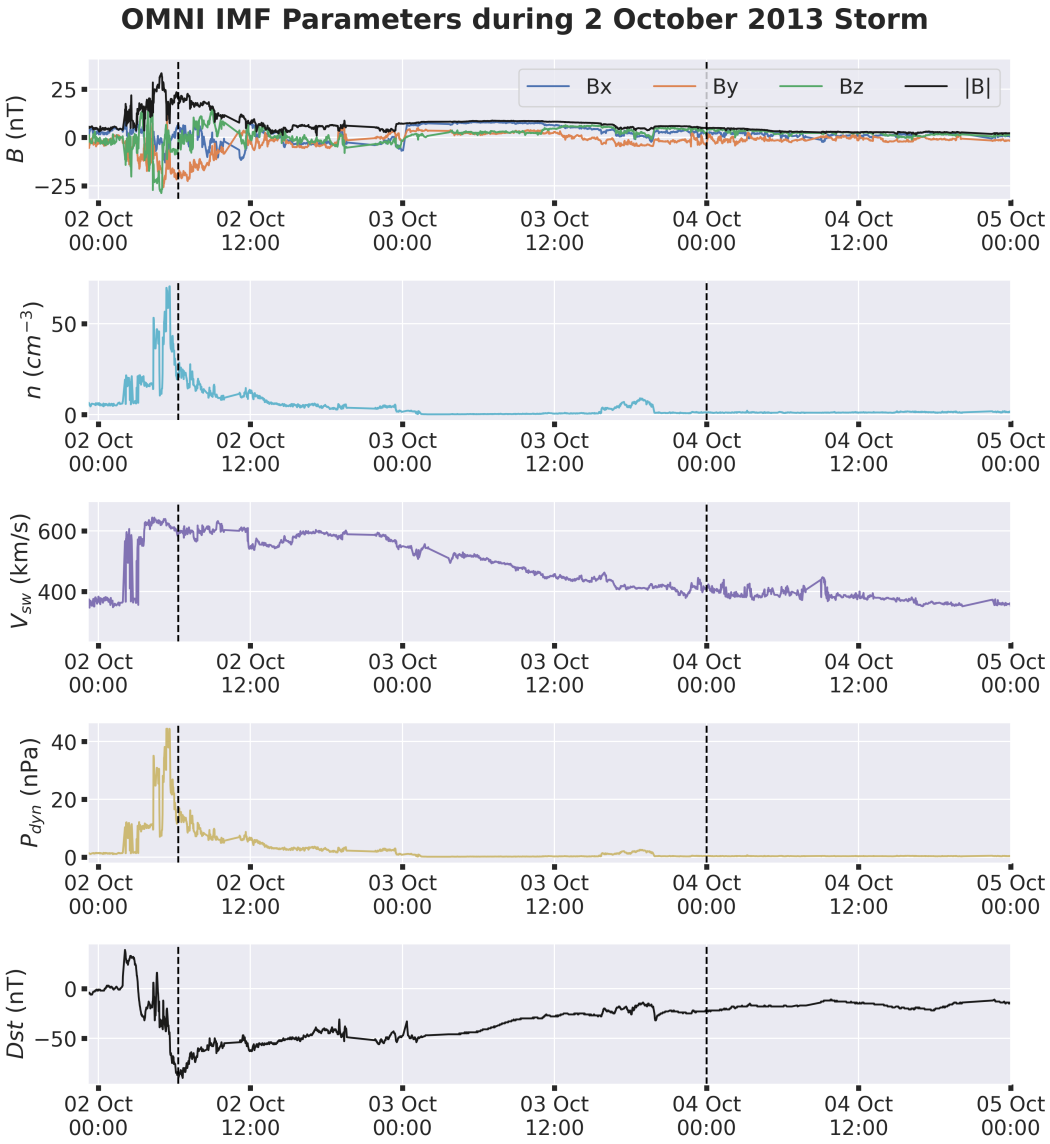

Figure A1. OMNI IMF Parameters during the 2 October 2013 storm. This data was taken from the OMNI database, which propagates satellite observations of the upstream solar wind at the L1 point to Earth's bow shock for geomagnetic storm analysis. The two vertical bars identify the minimum D_{st} (left vertical bar), and the quiet time period referenced in Figures 1 and 5.

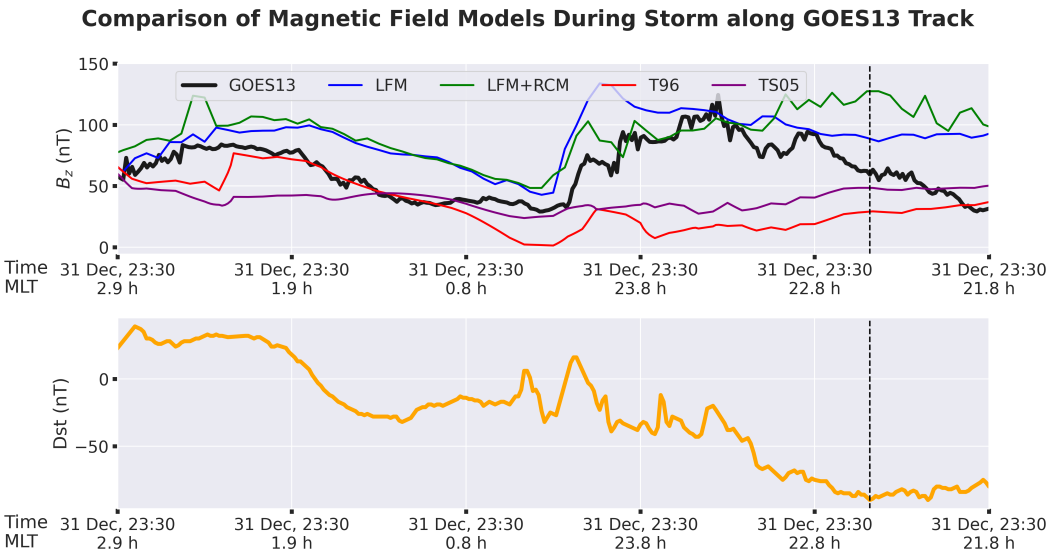

Figure B1. Zoomed Portion of 2 October 2013 Storm during the main phase of the storm (up until and slightly after D_{st} minimum). In this plot, we notice that the shape of B_z observed by GOES-13 is much better captured by the MHD models (LFM and LFM-RCM) than by the empirical models (T96 and TS05). Up until around 10/02 04:30, all models show a gradual decrease in B_z, though the arc is more closely captured by the MHD models. However, only the MHD models capture the increase in B_z following this period. In the final hour of this plot, GOES-13 observations show B_Z reducing again, which is captured well by no model.

lines are isolines of magnetic field intensity, drawn at cubically decreasing intensity levels.

We recall that particles with 90° pitch angles will orbit along isolines of B_{min}. However, in this plot we see that night-side "islands" of magnetic field intensity exist in the equatorial plane which would prevent such a trajectory from making a complete orbit around the earth. The drift shell calculation description in *Section 2 - Algorithms and Methods* describes visiting each magnetic local time under the assumption that a full orbit is made. However, in a field such as this that will not be the case.

Furthermore, on the dayside, there exist "reversals" in the equatorial magnetic field intensity isolines that conflict with the drift shell calculation. The drift shell calculation assumes that each magnetic local time is only visited once, allowing the drift shell to be convex. If the isolines of B reverse direction, the drift shell becomes concave and calculating one drift shell distance for that magnetic local time is no longer sufficient.

Appendix D Evaluation of Alternatives: IGRF and 2D Polar Cap Integration

In this Appendix section, we evaluate alternatives to the methods presented in this manuscript. Previous works such as Selesnick & Blake (2000) have suggested that IGRF may be important to the calculation of L^*, and other works such as Albert et al. (2018) suggest that L* be calculated through a 2D integration over the polar cap using the equation $L^* = 2\pi k_0/(\Phi R_E)$, where k_0 is Earth's dipole moment, and $\Phi = \iint \mathbf{B} \cdot \hat{\mathbf{n}}\, dA$ as in Equation 7. This is in contrast to the modified Roederer & Zhang (2016) equation 3.40 presented in Equation 5, whose derivation starts with the 2D integral form of Φ,

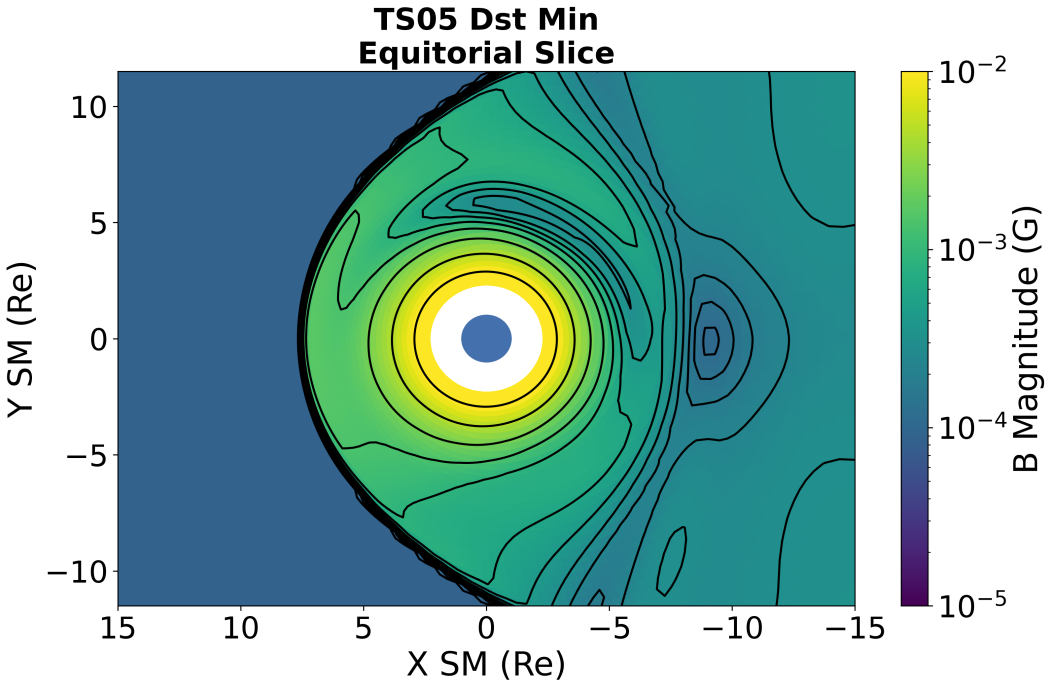

Figure C1. An example of a non-closed drift shell, which exhibits at least two features which complicate the calculation of the drift shell and in turn L^*. First, night-side "islands" of equatorial magnetic field intensity exist on the nightside, which would prevent particles mirroring at B_{min} from making a full orbit around earth. Secondly, on the dayside there exist reversals in the direction of the equatorial magnetic field intensity isolines which prevent the drift shell from being convex (a condition required for our algorithm).

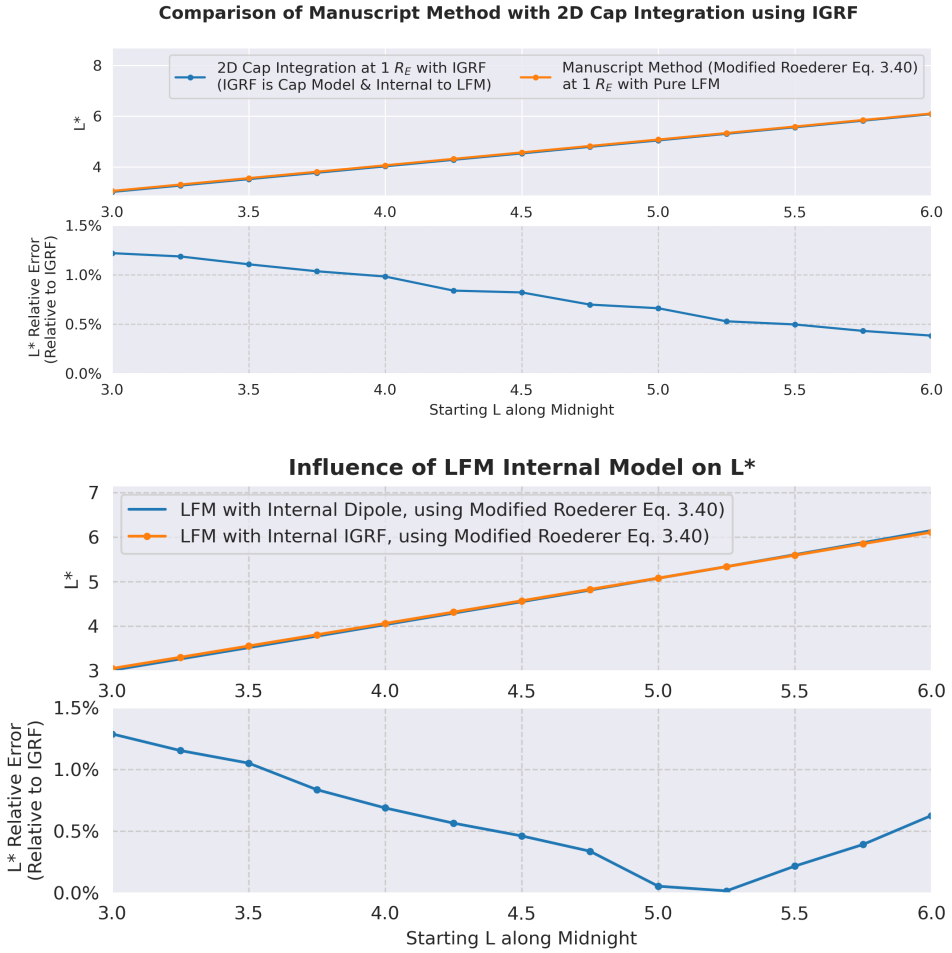

Figure D1. Top panel: Demonstration that using the 2D Polar Cap integration method with the LFM internal model changed to IGRF as a post-processing step has a negligible impact on L^* ($< 1.5\%$) for $3 \leq L \leq 6$ compared to using the method presented in this manuscript. Bottom panel: Demonstration without using the 2D polar cap integration, that the effect of changing the LFM internal model to IGRF as a post-processing step has a negligible impact on L^* ($< 1.5\%$) for $3 \leq L \leq 6$ compared to using LFM with an internal dipole (the official method of this manuscript).

applies the dipole model to provide **B** (Roederer & Zhang, 2016), and is modified against using the dipole model to extend each footpoint from the model inner boundary to Earth's surface (a contribution of this work).

IGRF is an empirical model of Earth's internal magnetic field designed to capture deviations from the dipole and drifts in the magnetic structure over time. We investigate using IGRF in two ways. First, we evaluate IGRF serving as an internal model for LFM, wherein the for each point on the model grid the dipole field is subtracted and the IGRF field is added to replace it as a post-processing step. We note that this results in more realistic non-dipiolar near-Earth fields for the L^* calculation, but also removes the consistency of the fields with the MHD model physics used to produce them (which assume an internal dipole). Second, we evaluate using IGRF to trace each drift shell footpoint at the model inner boundary down to Earth's surface, at which point the 2D integration over the polar cap would be performed.

An experiment is performed to evaluate the effect of doing both these alternatives at the same time. The results are displayed in the top panel of Figure D1. To perform the 2D polar cap integration at 1 R_E, we numerically integrated,

$$\Phi = \int_{\phi=0}^{\phi=2\pi} \int_{\theta=\theta_{surface}(\phi)}^{\theta=\pi/2} B_r \sin(\theta) R_E^2 d\theta d\phi, \tag{D1}$$

where B_r is the radial magnetic field component, and $\theta_{surface}$ is the colatitude of the point which results from tracing the drift shell footpoint at the model inner boundary down to Earth's surface using IGRF. In this experiment, it is found for $3 \leq L \leq 6$ the difference in L^* between these two methods is within 1.5%. This was deemed a very small change which did not outweigh the cost associated with integrating IGRF into the final software and causing our results to now depend on the details of another model.

We further seek to understand whether spatial variations in the IGRF field strength are impactful to the calculation. To further check this, an experiment is performed where the 2D integration method is applied to produce L^* corresponding to artificial circular polar caps spanning varying magnetic latitudes. The calculation is repeated with **B** provided by the standard dipole model and then again with IGRF. It was found that for polar caps extending between 30° and 60° MLAT, the difference between L^* calculated each way is less than 1.5%.

Furthermore, a calculation of the dipole strength of IGRF using the 2010 coefficients and Equation 6 of Alken et al. (2021) produced a value of $B_0^{IGRF} = 29,950.126$ nT, which is within 0.2% of LFM's nominal $B_0^{LFM} = 30,000$ nT. However, we note that the IGRF dipole strength drifts year-by-year, and has drifted on the order of 5% between the years of 1900 to 2000.

A final experiment was performed to check the effect of replacing the LFM internal model with IGRF as a post-processing step, while holding the L^* equation unchanged. That was done to separate the effects of the 2D polar cap integration method from using IGRF as the internal model. The results are displayed in the bottom panel of Figure D1. It was found that when this the internal model was changed this way, the difference in L^* was again less than 1.5%. For the same reasons as before, this difference was deemed too small to be worth the cost.

References

Albert, J. M., Selesnick, R., Morley, S. K., Henderson, M. G., & Kellerman, A. (2018). Calculation of last closed drift shells for the 2013 gem radiation belt challenge events. *Journal of Geophysical Research: Space Physics*, *123*(11), 9597–9611.

Alken, P., Thébault, E., Beggan, C. D., Amit, H., Aubert, J., Baerenzung, J., ... others (2021). International geomagnetic reference field: the thirteenth generation. *Earth, Planets and Space*, *73*(1), 1–25.

Allison, H. J., Shprits, Y. Y., Zhelavskaya, I. S., Wang, D., & Smirnov, A. G. (2021). Gyroresonant wave-particle interactions with chorus waves during extreme depletions of plasma density in the van allen radiation belts. *Science Advances*, *7*(5), eabc0380.

Artemyev, A., Agapitov, O., Mourenas, D., Krasnoselskikh, V., & Zelenyi, L. (2013). Storm-induced energization of radiation belt electrons: Effect of wave obliquity. *Geophysical Research Letters*, *40*(16), 4138–4143.

Baker, D. (1998). What is space weather? *Advances in Space Research*, *22*(1), 7–16.

Baker, D., Allen, J., Kanekal, S., & Reeves, G. (1998). Disturbed space environment may have been related to pager satellite failure. *Eos, Transactions American Geophysical Union*, *79*(40), 477–483.

Baker, D., Kanekal, S., Blake, J., Klecker, B., & Rostoker, G. (1994). Satellite anomalies linked to electron increase in the magnetosphere. *Eos, Transactions American Geophysical Union*, *75*(35), 401–405.

Bard, C. M., & Dorelli, J. C. (2021). Magnetotail reconnection asymmetries in an ion-scale, earth-like magnetosphere. In *Annales geophysicae* (Vol. 39, pp. 991–1003).

Boyd, A. J., Turner, D., Reeves, G. D., Spence, H., Baker, D., & Blake, J. (2018). What causes radiation belt enhancements: A survey of the van allen probes era. *Geophysical Research Letters*, *45*(11), 5253–5259.

Chen, F. F., et al. (1984). *Introduction to plasma physics and controlled fusion* (Vol. 1). Springer.

Dormand, J. R., & Prince, P. J. (1980). A family of embedded runge-kutta formulae. *Journal of computational and applied mathematics*, *6*(1), 19–26.

Elkington, S. R., Hudson, M. K., & Chan, A. A. (2003). Resonant acceleration and diffusion of outer zone electrons in an asymmetric geomagnetic field. *Journal of Geophysical Research: Space Physics*, *108*(A3).

Elkington, S. R., Hudson, M. K., Wiltberger, M. J., & Lyon, J. G. (2002). Mhd/particle simulations of radiation belt dynamics. *Journal of atmospheric and solar-terrestrial physics*, *64*(5-6), 607–615.

Escoubet, C., Fehringer, M., & Goldstein, M. (2001). Introduction the cluster mission. In *Annales geophysicae* (Vol. 19, pp. 1197–1200).

Fehlberg, E. (1969). Classical fifth-and seventh-order runge-kutta formulas with stepsize control. *Computing*, *4*, 93–106.

Fei, Y., Chan, A. A., Elkington, S. R., & Wiltberger, M. J. (2006). Radial diffusion and mhd particle simulations of relativistic electron transport by ulf waves in the september 1998 storm. *Journal of Geophysical Research: Space Physics*, *111*(A12).

Fitzpatrick, R. (2022). *Plasma physics: an introduction*. Crc Press.

Gloeckler, G., Balsiger, H., Bürgi, A., Bochsler, P., Fisk, L., Galvin, A., ... others (1995). The solar wind and suprathermal ion composition investigation on the wind spacecraft. *Space Science Reviews*, *71*, 79–124.

Green, J. C., & Kivelson, M. (2004). Relativistic electrons in the outer radiation belt: Differentiating between acceleration mechanisms. *Journal of Geophysical Research: Space Physics*, *109*(A3).

Haerendel, G. (1968). *Diffusion theory of trapped particles and the observed proton distribution.* (Tech. Rep.). Max-Planck-Institut fuer Physik und Astrophysik, Garching, Ger.

Heinemann, M., & Wolf, R. (2001). Relationships of models of the inner magnetosphere to the rice convection model. *Journal of Geophysical Research: Space*

Physics, *106*(A8), 15545–15554.

Henderson, M., Morley, S., Niehof, J., & Larsen, B. (2018, March). *drsteve/lanlgeomag: v1.5.16.* Zenodo. Retrieved from `https://doi.org/10.5281/zenodo.1195041` doi: 10.5281/zenodo.1195041

Huba, J. (1995). Hall magnetohydrodynamics in space and laboratory plasmas. *Physics of Plasmas*, *2*(6), 2504–2513.

Ingraham, J., Cayton, T., Belian, R., Christensen, R., Friedel, R., Meier, M., ... Tuszewski, M. (2001). Substorm injection of relativistic electrons to geosynchronous orbit during the great magnetic storm of march 24, 1991. *Journal of Geophysical Research: Space Physics*, *106*(A11), 25759–25776.

Kallenrode, M.-B. (2004). *Space physics: an introduction to plasmas and particles in the heliosphere and magnetospheres.* Springer Science & Business Media.

Konstantinidis, K., & Sarris, T. (2015). Calculations of the integral invariant coordinates i and l* in the magnetosphere and mapping of the regions where i is conserved, using a particle tracer (ptr3d v2. 0), lanl*, spenvis, and irbem. *Geoscientific Model Development*, *8*(9).

Kos, L., Pitts, R., Simič, G., Brank, M., Anand, H., & Arter, W. (2019). Smiter: A field-line tracing environment for iter. *Fusion Engineering and Design*, *146*, 1796–1800.

Langel, R. (1992). International geomagnetic reference field the sixth generation. *Journal of geomagnetism and geoelectricity*, *44*(9), 679–707.

Li, Z., Hudson, M., Patel, M., Wiltberger, M., Boyd, A., & Turner, D. (2017). Ulf wave analysis and radial diffusion calculation using a global mhd model for the 17 march 2013 and 2015 storms. *Journal of Geophysical Research: Space Physics*, *122*(7), 7353–7363.

Lyon, J., Fedder, J., & Mobarry, C. (2004). The lyon–fedder–mobarry (lfm) global mhd magnetospheric simulation code. *Journal of Atmospheric and Solar-Terrestrial Physics*, *66*(15-16), 1333–1350.

Mauk, B., Fox, N. J., Kanekal, S., Kessel, R., Sibeck, D., & Ukhorskiy, a. A. (2014). Science objectives and rationale for the radiation belt storm probes mission. *The van allen probes mission*, 3–27.

McCollough, J., Elkington, S., & Baker, D. (2012). The role of shabansky orbits in compression-related electromagnetic ion cyclotron wave growth. *Journal of Geophysical Research: Space Physics*, *117*(A1).

Murphy, J. J. (2017). *Advanced analysis and visualization of space weather phenomena* (Unpublished doctoral dissertation). University of Colorado at Boulder.

Northrop, T. G. (1963). Adiabatic charged-particle motion. *Reviews of Geophysics*, *1*(3), 283–304.

Olsen, N., Sabaka, T. J., & Tøoffner-Clausen, L. (2000). Determination of the igrf 2000 model. *Earth, planets and space*, *52*(12), 1175–1182.

Raeder, J., Larson, D., Li, W., Kepko, E. L., & Fuller-Rowell, T. (2008). Openggcm simulations for the themis mission. *Space Science Reviews*, *141*, 535–555.

Reeves, G., Spence, H. E., Henderson, M., Morley, S., Friedel, R., Funsten, H., ... others (2013). Electron acceleration in the heart of the van allen radiation belts. *Science*, *341*(6149), 991–994.

Roederer, J. G., & Zhang, H. (2016). *Dynamics of magnetically trapped particles.* Springer.

Sarris, T. E., Li, X., Zhao, H., Khoo, L. Y., Liu, W., & Temerin, M. A. (2021). On the association between electron flux oscillations and local phase space density gradients. *Journal of Geophysical Research: Space Physics*, *126*(2), e2020JA028891.

Schulz, M. (1996). Canonical coordinates for radiation-belt modeling. *Radiation Belts: Models and Standards*, *97*, 153–160.

Schulz, M., & Lanzerotti, L. J. (1974). *Particle diffusion in the radiation belts.* doi:

10.1007/978-3-642-65675-0

Selesnick, R., & Blake, J. (2000). On the source location of radiation belt relativistic electrons. *Journal of Geophysical Research: Space Physics*, *105*(A2), 2607–2624.

Shabansky, V. (1971). Some processes in the magnetosphere. *Space Science Reviews*, *12*, 299–418.

Shea, M., & Smart, D. (1998). Space weather: The effects on operations in space. *Advances in Space Research*, *22*(1), 29–38.

Toffoletto, F., Sazykin, S., Spiro, R., & Wolf, R. (2003). Inner magnetospheric modeling with the rice convection model. *Space science reviews*, *107*, 175–196.

Tóth, G., Van der Holst, B., Sokolov, I. V., De Zeeuw, D. L., Gombosi, T. I., Fang, F., ... others (2012). Adaptive numerical algorithms in space weather modeling. *Journal of Computational Physics*, *231*(3), 870–903.

Tsyganenko, N. (1995). Modeling the earth's magnetospheric magnetic field confined within a realistic magnetopause. *Journal of Geophysical Research: Space Physics*, *100*(A4), 5599–5612.

Tsyganenko, N. (2002). A model of the near magnetosphere with a dawn-dusk asymmetry 1. mathematical structure. *Journal of Geophysical Research: Space Physics*, *107*(A8), SMP–12.

Tsyganenko, N., & Sitnov, M. (2005). Modeling the dynamics of the inner magnetosphere during strong geomagnetic storms. *Journal of Geophysical Research: Space Physics*, *110*(A3).

Tsyganenko, N., & Sitnov, M. (2007). Magnetospheric configurations from a high-resolution data-based magnetic field model. *Journal of Geophysical Research: Space Physics*, *112*(A6).

Tsyganenko, N. A. (1989). A magnetospheric magnetic field model with a warped tail current sheet. *Planetary and Space Science*, *37*(1), 5–20.

Tu, W., Selesnick, R., Li, X., & Looper, M. (2010). Quantification of the precipitation loss of radiation belt electrons observed by sampex. *Journal of Geophysical Research: Space Physics*, *115*(A7).

Ukhorskiy, A., Takahashi, K., Anderson, B., & Korth, H. (2005). Impact of toroidal ulf waves on the outer radiation belt electrons. *Journal of Geophysical Research: Space Physics*, *110*(A10).

Virtanen, P., Gommers, R., Oliphant, T. E., Haberland, M., Reddy, T., Cournapeau, D., ... others (2020). Scipy 1.0: fundamental algorithms for scientific computing in python. *Nature methods*, *17*(3), 261–272.

Walsh, A. P., Haaland, S., Forsyth, C., Keesee, A. M., Kissinger, J., Li, K., ... others (2014). Dawn–dusk asymmetries in the coupled solar wind–magnetosphere–ionosphere system: A review. In *Annales geophysicae* (Vol. 32, pp. 705–737).

Wiltberger, M., Pulkkinen, T., Lyon, J., & Goodrich, C. (2000). Mhd simulation of the magnetotail during the december 10, 1996, substorm. *Journal of Geophysical Research: Space Physics*, *105*(A12), 27649–27663.

Yu, Y., Koller, J., Zaharia, S., & Jordanova, V. (2012). L* neural networks from different magnetic field models and their applicability. *Space Weather*, *10*(2).

Zhang, B., Sorathia, K. A., Lyon, J. G., Merkin, V. G., Garretson, J. S., & Wiltberger, M. (2019). Gamera: A three-dimensional finite-volume mhd solver for non-orthogonal curvilinear geometries. *The Astrophysical Journal Supplement Series*, *244*(1), 20.